



# Combined emergent constraints on future extreme precipitation changes

Received: 26 January 2025

Accepted: 22 May 2025

Published online: 19 June 2025

Check for updates

Hideo Shiogama <sup>1</sup>, Michiya Hayashi <sup>1</sup>, Nagio Hirota <sup>1</sup>, Tomoo Ogura <sup>1</sup>, Hyungjun Kim <sup>2,3,4,5</sup> & Masahiro Watanabe <sup>6</sup>

Recent studies have shown that the observed global warming trend over recent decades provides efficient constraints not only for future global mean temperature increases ( $\Delta T_{gm}$ ) across Earth system models but also for changes in several climate variables that include significant  $\Delta T_{gm}$ -related uncertainty. However,  $\Delta T_{gm}$ -related emergent constraints (ECs) cannot reduce the uncertainty unrelated to  $\Delta T_{gm}$ . Here, to overcome this limitation, we develop an EC method and apply it to future changes in the annual maximum daily precipitation in order to reduce uncertainty therein. An EC for precipitation sensitivity based on historical extreme precipitation biases is combined with the constrained  $\Delta T_{gm}$ . This combined EC decreases the variance of the global mean precipitation by 42%, an improvement from only using temperature (resulting in 26% reduction), and the variance of regional precipitation by  $\geq 30\%$  in 24% of the globe (whereas  $\geq 30\%$  reduction is only seen in 2% of the globe with the temperature-related EC).

Changes in extreme heavy precipitation throughout various regions of the world are of considerable interest due to their damage to social and natural systems<sup>1,2</sup>. Global economic losses resulting from floods reached USD 82 billion in 2021<sup>3</sup>. Anthropogenic signals have been detected in historical changes in precipitation extremes<sup>2,4–6</sup>, and future increases in the frequency and intensity of heavy-precipitation extremes are projected<sup>2,7–12</sup>. To inform climate policies, it is important to reduce differences (uncertainty) in climate change projections across Earth system models (ESMs), even though ESMs do not necessarily capture uncertainties fully<sup>13</sup>.

As a promising approach to reduce uncertainty, emergent constraints (ECs) have been actively studied for nearly 20 years<sup>13–17</sup>. In the studies of ECs, it is necessary to obtain statistically and physically reasonable relationships between a current climate metric and future change across ESMs, and then compare current climate simulations with observations to evaluate the reliability of the future projections and reduce the uncertainty ranges. Previous studies<sup>18–21</sup> have succeeded in reducing the uncertainty in future global mean temperature

changes ( $\Delta T_{gm}$ ) via the use of a positive correlation between  $\Delta T_{gm}$  and recent trends (e.g., after 1970) in the global mean temperature ( $trT_{gm}$ ).

Reference<sup>22</sup> reported that  $trT_{gm}$  can also be employed to constrain future global mean precipitation changes because future global mean precipitation changes are clearly proportional to  $\Delta T_{gm}$  (8–30% reductions of the variance). This finding suggests the possibility of constraining the uncertainty in changes in other climate variables by using  $trT_{gm}$  if the changes in those variables are proportional to  $\Delta T_{gm}$  and  $trT_{gm}$ . In other words, ECs on  $\Delta T_{gm}$  can propagate to uncertainty constraints on other variables<sup>23</sup>. On the basis of this concept, recent studies have constrained uncertainties in future global and regional changes in extreme precipitation<sup>23–26</sup>, extreme temperature, surface longwave radiation, specific humidity<sup>23</sup> and the carbon cycle in the Amazon region<sup>27</sup> by using their relationships with  $\Delta T_{gm}$  (and  $trT_{gm}$ ). The economic impact of climate change was also constrained based on this idea<sup>28</sup>.

Although the studies of  $\Delta T_{gm}$ -related ECs on several variables have exhibited major progress, the limitation is that  $\Delta T_{gm}$ -related ECs

<sup>1</sup>Earth System Division, National Institute for Environmental Studies, Tsukuba, Japan. <sup>2</sup>Moon Soul Graduate School of Future Strategy, Korea Advanced Institute of Science and Technology, Daejeon, Korea. <sup>3</sup>Department of Civil and Environmental Engineering, Korea Advanced Institute of Science and Technology, Daejeon, Korea. <sup>4</sup>Graduate School of Green Growth and Sustainability, Korea Advanced Institute of Science and Technology, Daejeon, Korea.

<sup>5</sup>Graduate School of Data Science, Korea Advanced Institute of Science and Technology, Daejeon, Korea. <sup>6</sup>Atmosphere and Ocean Research Institute, University of Tokyo, Kashiwa, Japan. e-mail: [shiogama.hideo@nies.go.jp](mailto:shiogama.hideo@nies.go.jp)

cannot reduce  $\Delta T_{gm}$ -unrelated uncertainties. To overcome this limitation, here we develop a method to combine  $\Delta T_{gm}$ -related and  $\Delta T_{gm}$ -unrelated ECs. Our idea is simple. We denote future changes in a variable  $X$  as  $\Delta X$ , and consider the following:

$$\Delta X = \frac{\Delta X}{\Delta T_{gm}} \Delta T_{gm} \quad (1)$$

where  $\frac{\Delta X}{\Delta T_{gm}}$  is the sensitivity of  $\Delta X$  per 1°C of global warming (i.e., the  $\Delta T_{gm}$ -unrelated component). If  $\Delta X$  is correlated with  $\Delta T_{gm}$ , we can apply the  $\Delta T_{gm}$ -related EC to  $\Delta X^{22-28}$ . Furthermore, if we can propose an EC on  $\frac{\Delta X}{\Delta T_{gm}}$ , we can statistically combine the EC on  $\frac{\Delta X}{\Delta T_{gm}}$  and the EC on  $\Delta T_{gm}$  to reduce the uncertainty in  $\Delta X$ . We apply this idea of a combined EC to global and regional changes in the annual maximum daily precipitation, which is an important indicator for impact assessments. First, we propose an EC on the sensitivity of the annual maximum daily precipitation, and then reveal that the combined EC can efficiently reduce the uncertainty in annual maximum daily precipitation changes compared with the  $\Delta T_{gm}$ -related EC only.

## Results

### ECs on the global mean changes in single variables

We mainly analyze the historical and RCP4.5/SSP2-4.5 simulations of 56 ESMs of the Phase 5 of the Coupled Model Intercomparison Project (CMIP5)<sup>29</sup> and CMIP6<sup>30,31</sup> ensembles (Supplementary Table 1, "Methods"). RCP4.5/SSP2-4.5 represents a medium trajectory for greenhouse gas emissions.

In Fig. 1, we investigate future changes in the global average annual maximum daily precipitation ( $\Delta R_{gm}$ ), the annual mean temperature ( $\Delta T_{gm}$ ) and the sensitivity of the annual maximum daily precipitation per 1°C of global warming ( $\frac{\Delta R_{gm}}{\Delta T_{gm}}$ ). Here,  $\Delta$  indicates 2051–2100 minus 1851–1900, and the suffix "gm" denotes the global mean. Because anthropogenic aerosol emissions are small in both the periods of 2051–2100 and 1851–1900<sup>29–31</sup>,  $\Delta T_{gm}$  and  $\Delta R_{gm}$  (2051–2100 minus 1851–1900) are mainly forced by increases in greenhouse gas concentrations<sup>19,22,23</sup>. We define  $trT_{gm}$  as the recent past (1970–2022) global mean temperature trends. Because global aerosol emissions were nearly constant in this period, the aerosol forcing has little effect on  $trT_{gm}$ <sup>18,19</sup>.  $\Delta R_{gm}$  and  $\Delta T_{gm}$  are significantly correlated with  $trT_{gm}$ <sup>18–26</sup> ( $r=0.55$  and  $0.76$ ) (Fig. 1a, b), because all  $\Delta R_{gm}$ ,  $\Delta T_{gm}$  and  $trT_{gm}$  are mainly driven by increases of greenhouse gas concentrations (Methods). We apply the hierarchical EC framework<sup>32</sup> to reduce uncertainties in future changes of single variables (Methods). By comparing the simulated  $trT_{gm}$  values with the observations (HadCRUT5<sup>33</sup>), we can reduce the inter-model variance in  $\Delta R_{gm}$  (the relative reduction of variance (RRV) is 26%) and  $\Delta T_{gm}$  (RRV = 51%), as shown by the previous studies<sup>18–26</sup>. Here, we consider the uncertainties in the observed  $trT_{gm}$  due to the internal climate variability and the spread of 200 realizations of HadCRUT5 (Methods). It has been suggested that the EC on  $\Delta T_{gm}$  can be affected by the internal variability component of the tropical Pacific surface warming pattern<sup>34</sup>. However, the relative contributions of forced changes and internal variability to the observed tropical Pacific surface warming pattern are highly uncertain<sup>35</sup>. Therefore, as a sensitivity test, we double the variance in the internal climate variability added to the observed  $trT_{gm}$ <sup>28</sup> and redo the EC calculations. Our results remain robust (Fig. 1a, b).

We find that  $\frac{\Delta R_{gm}}{\Delta T_{gm}}$  correlates well with the 1997–2019 mean  $R_{gm}$  ( $r=0.74$ ): ESMs with larger  $R_{gm}$  values under the present climate condition tend to exhibit greater  $\frac{\Delta R_{gm}}{\Delta T_{gm}}$  (Fig. 1c). Here we analyze the 1997–2019 mean  $R_{gm}$  instead of the 1851–1900 mean value because of the limited availability of observational datasets (GPCP<sup>36</sup>, MSWEP2<sup>37</sup> and GSWP3-W5ES<sup>38,39</sup>). It is confirmed that the 1997–2019 mean  $R_{gm}$  values are close to the 1851–1900 mean values (Supplementary Fig. 1a).

By applying the EC method ("Methods"), we can reduce the variance in  $\frac{\Delta R_{gm}}{\Delta T_{gm}}$  by 36% (Fig. 1c). The central value and the lower and upper bounds of  $\frac{\Delta R_{gm}}{\Delta T_{gm}}$  (mm/day/°C), estimated as the 50th [2.5th, 97.5th] percentile values, are 2.07 [0.316, 3.82] for the raw ensembles and 2.03 [0.632, 3.44] for the constrained range. The EC does not drastically alter the 50th percentile values (only  $-0.04$ ), but changes lower (+0.316) and upper bounds ( $-0.38$ ).

The mechanism underlying the significant correlation between  $\frac{\Delta R_{gm}}{\Delta T_{gm}}$  and the present climatology of  $R_{gm}$  cannot be simply explained by the Clausius-Clapeyron relationship (i.e.,  $\frac{\Delta R_{gm}}{\Delta T_{gm}} \approx 7(\%/\text{°C}) \times$  the present climatology of  $R_{gm}$ ) (Fig. 1c). The regression line between  $\frac{\Delta R_{gm}}{\Delta T_{gm}}$  and the present climatology of  $R_{gm}$  does not exhibit a slope of 7%/°C. This relationship is caused by inter-model variations in the sensitivity of  $R$  to humidity as discussed later.

### Combined ECs

The  $\Delta T_{gm}$ -related uncertainty in  $\Delta R_{gm}$  was reduced in Fig. 1a (we refer to this as "the  $\Delta T_{gm}$ -related EC on  $\Delta R_{gm}$ "). By applying the hierarchical EC framework<sup>32</sup>, we also constrained the  $\Delta T_{gm}$ -unrelated uncertainty in  $\frac{\Delta R_{gm}}{\Delta T_{gm}}$  in Fig. 1c. To investigate the effects of the constrained  $\frac{\Delta R_{gm}}{\Delta T_{gm}}$  for the uncertainty reduction of  $\Delta R_{gm}$ , we develop the following method that uses the information of the constrained  $\frac{\Delta R_{gm}}{\Delta T_{gm}}$  and the raw  $\Delta T_{gm}$ . By assuming normal distributions for both the constrained  $\frac{\Delta R_{gm}}{\Delta T_{gm}}$  and the raw  $\Delta T_{gm}$ , we can estimate the joint normal distribution of the combination of the constrained  $\frac{\Delta R_{gm}}{\Delta T_{gm}}$  and the raw  $\Delta T_{gm}$  (Supplementary Fig. 2). We randomly sample  $\frac{\Delta R_{gm}}{\Delta T_{gm}}, \Delta T_{gm}$  from this joint normal distribution and then calculate  $\Delta R_{gm} = \frac{\Delta R_{gm}}{\Delta T_{gm}} \Delta T_{gm}$  10000 times. By using the distribution of the 10000  $\Delta R_{gm}$  samples, we estimate the probability density function (PDF) of

$$\left( \text{constrained } \Delta R_{gm} \text{ related to } \frac{\Delta R_{gm}}{\Delta T_{gm}} \right) = \left( \text{constrained } \frac{\Delta R_{gm}}{\Delta T_{gm}} \right) \times (\text{raw } \Delta T_{gm}) \quad (2)$$

We refer to this method as "the  $\frac{\Delta R_{gm}}{\Delta T_{gm}}$ -related EC on  $\Delta R_{gm}$ " ("Methods").

In the next step, by combining the constrained  $\frac{\Delta R_{gm}}{\Delta T_{gm}}$  (Fig. 1c) and the constrained  $\Delta T_{gm}$  (Fig. 1b and Supplementary Fig. 2), we also obtain their joint normal distribution, and then calculate the PDF of

$$(constrained \Delta R_{gm}) = \left( \text{constrained } \frac{\Delta R_{gm}}{\Delta T_{gm}} \right) \times (\text{constrained } \Delta T_{gm}) \quad (3)$$

This method is referred to as "the combined EC on  $\Delta R_{gm}$ " ("Methods").

Figure 2 and Table 1 show the raw and constrained PDFs of  $\Delta R_{gm}$  and the corresponding uncertainty ranges (mm/day). The  $\Delta T_{gm}$ -related EC mainly lowers the upper bound of  $\Delta R_{gm}$  (changed from 5.49 [0.025, 10.9] to 5.15 [0.467, 9.83]). On the other hand, the  $\frac{\Delta R_{gm}}{\Delta T_{gm}}$ -related EC mainly raises the lower bound of  $\Delta R_{gm}$  (the constrained range is 5.13 [1.36, 10.5]). These  $\Delta T_{gm}$ -related and  $\frac{\Delta R_{gm}}{\Delta T_{gm}}$ -related ECs reduce the variance in  $\Delta R_{gm}$  by 26% and 27%, respectively. By applying the combined EC method, we can decrease the upper bound, increase the lower bound (the constrained range is 5.02 [1.44, 9.84]) and reduce the

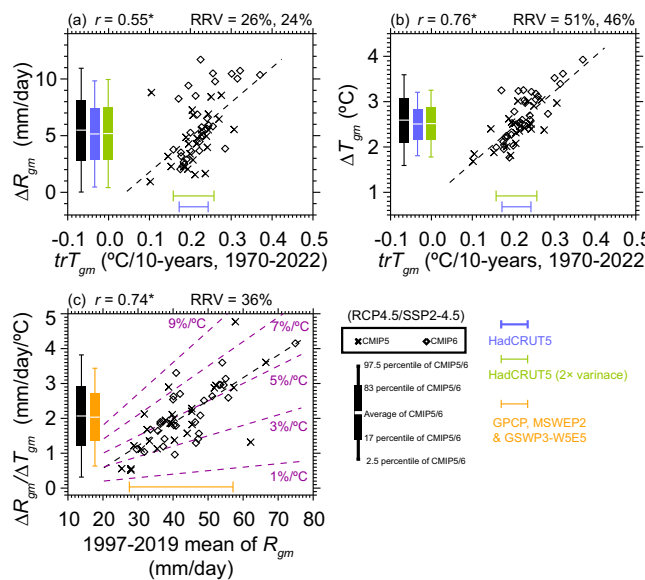


**Fig. 1 | Emergent constraints on global mean extreme precipitation change ( $\Delta R_{gm}$ ), temperature change ( $\Delta T_{gm}$ ) and extreme precipitation sensitivity ( $\frac{\Delta R_{gm}}{\Delta T_{gm}}$ ).** Vertical axes indicate (a)  $\Delta R_{gm}$  (2051–2100 minus 1851–1900, mm/day), (b)  $\Delta T_{gm}$  (°C) and (c)  $\frac{\Delta R_{gm}}{\Delta T_{gm}}$  (mm/day/°C), respectively. Horizontal axes show the recent past (1970–2022) global mean temperature trends ( $trT_{gm}$ , °C/10-years) for the top panels and the 1997–2019 mean  $R_{gm}$  for the bottom one. Crosses and diamonds denote the CMIP5 and CMIP6 models (ensemble mean of each model), respectively. Pearson's correlations ( $r$ ) and relative reduction of variance (RRV) are provided at the top of the panels. Asterisks indicate that those correlations are significant at the 5% level. Black dashed lines show the linear regressions. Purple dashed lines of the panel (c) denote the 1–95% values of the 1997–2019 mean  $R_{gm}$ . Horizontal bars of the top panels indicate the 2.5–97.5% ranges of HadCRUT5 (blue) and that with doubled variance of the internal variability (green). Horizontal bar of the panel (c) shows the 2.5–97.5% range of  $R_{gm}$  estimated from the GPCP, MSWEP2 and GSWP3-WSE5 data. Vertical box plots show the raw uncertainty ranges of the models (black) and the constrained ranges using the observations (colors).

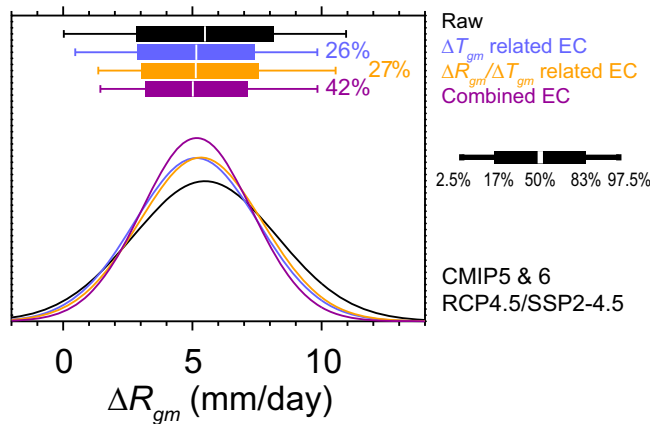


**Fig. 2 | Emergent constraints on global mean extreme precipitation change ( $\Delta R_{gm}$ ).** The black curve and box plot show the probability density function (PDF) of the raw  $\Delta R_{gm}$  (2051–2100 minus 1851–1900, mm/day) and the corresponding uncertainty range, respectively. Colored curves and box plots indicate the observational constrained PDFs and the corresponding uncertainty ranges based on (blue) the temperature-related emergent constraint ( $\Delta T_{gm}$ -related EC), (orange) the sensitivity-related ( $\frac{\Delta R_{gm}}{\Delta T_{gm}}$ -related) EC and (purple) the combined EC, respectively.

variance by 42%, which is much larger than the RRV of the  $\Delta T_{gm}$ -related EC (26%) developed in previous studies<sup>22,23</sup>. The changes in the 50th percentile values are slight for all the EC methods (changes

**Table 1 | Raw and constrained ranges of global mean extreme precipitation change ( $\Delta R_{gm}$ , mm/day) and the relative reduction of variances (RRVs, %) (CMIP5&6, RCP4.5/SSP2-4.5)**

	50th percentile (mm/day)	2.5th percentile (mm/day)	97.5th percentile (mm/day)	RRV (%)
Raw	5.49	0.025	10.9	–
$\Delta T_{gm}$ -related EC	5.15	0.467	9.83	26
$\frac{\Delta R_{gm}}{\Delta T_{gm}}$ -related EC	5.13	1.36	10.5	27
Combined EC	5.02	1.44	9.84	42

from 5.49 (the raw) to 5.15 (the  $\Delta T_{gm}$ -related EC), 5.13 (the  $\frac{\Delta R_{gm}}{\Delta T_{gm}}$ -related EC) and 5.02 (the combined EC), because the ESM averaged values of  $trT_{gm}$  (0.220 °C/10-years) and the 1997–2019 mean  $R_{gm}$  (43.1 mm/day) are close to the mean values of the observations (0.208 °C/10-years and 42.3 mm/day) (also see Eq. 6 of Method).

If we ignored the dependence between multiple ECs, our combined methods could be overconfident<sup>40</sup>. Therefore we consider the correlation between  $\Delta T_{gm}$  and  $\frac{\Delta R_{gm}}{\Delta T_{gm}}$  ( $r_0 = 0.28$ ) in Eqs. 9 and 11 of Methods (Supplementary Fig. 2). If we set  $r_0 = 0$  (i.e., ignoring the dependence), the RRV of the combined method could be 51%, while the actual RRV is 42%. We avoided this overconfident estimation by considering the correlation between  $\Delta T_{gm}$  and  $\frac{\Delta R_{gm}}{\Delta T_{gm}}$ .

These results remain robust even when we employ only the CMIP5 or CMIP6 ESMs (Supplementary Fig. 3a, b), whereas the RRVs are larger in the CMIP6 ESMs than in the CMIP5 ESMs because the CMIP6 ensemble involves more ‘hot ESMs’ than the CMIP5 ensemble<sup>19,22,23,41,42</sup>. Even if we calculate  $trT_{gm}$  in a different period (1980–2022), the combined method can reduce the uncertainty more efficiently than the  $\Delta T_{gm}$ -related EC (Supplementary Fig. 3d). To assess the influences of outliers, we redo the EC calculations with each of the ESMs omitted<sup>40</sup>, confirming that the RRVs are not sensitive to the ESM sampling (Supplementary Fig. 3f). These analyses indicate the robustness of our results.

We also analyze a higher greenhouse gas concentration scenario (RCP8.5/SSP5-8.5) (Supplementary Fig. 3c and Supplementary Table 2). The raw and constrained ranges of  $\Delta R_{gm}$  (mm/day) are 8.87 [0.557, 17.2] (raw), 8.03 [0.708, 15.4] ( $\Delta T_{gm}$ -related EC), 8.30 [2.10, 16.7] ( $\frac{\Delta R_{gm}}{\Delta T_{gm}}$ -related EC) and 7.99 [2.13, 15.4] (Combined EC). The  $\Delta T_{gm}$ -related EC lowers the upper bounds from 17.2 to 15.4. The  $\frac{\Delta R_{gm}}{\Delta T_{gm}}$ -related EC raises the lower bounds from 0.557 to 2.10. The combined EC changes both lower (from 0.557 to 2.13) and upper (from 17.2 to 15.4) bounds. The 50th percentile values change slightly from 8.87 to 8.03 (the  $\Delta T_{gm}$ -related EC), 8.30 (the  $\frac{\Delta R_{gm}}{\Delta T_{gm}}$ -related EC) and 7.99 (the combined EC). The RRVs are 22%, 20% and 37% for the  $\Delta T_{gm}$ -related EC,  $\frac{\Delta R_{gm}}{\Delta T_{gm}}$ -related EC and combined EC, respectively.

### ECs on regional changes

Here, we apply our EC methods to regional changes in the annual maximum daily precipitation ( $\Delta R$ ) (“Methods”). Differences between the 1997–2019 mean regional  $R$  and the 1851–1900 mean one are small (Supplementary Fig. 1b, c). Supplementary Fig. 4a, b show the correlations between  $\Delta R$  and  $trT_{gm}$  and between  $\frac{\Delta R}{\Delta T_{gm}}$  and the 1997–2019 mean regional  $R$ , respectively.  $\Delta R$  and  $trT_{gm}$  exhibit significant positive correlations mainly in the extratropical Ocean and the surrounding coastal area<sup>23</sup>. Ref<sup>23</sup> found that changes in regional temperature and specific humidity are well related to  $\Delta T_{gm}$  ( $trT_{gm}$ ) in most of the world.

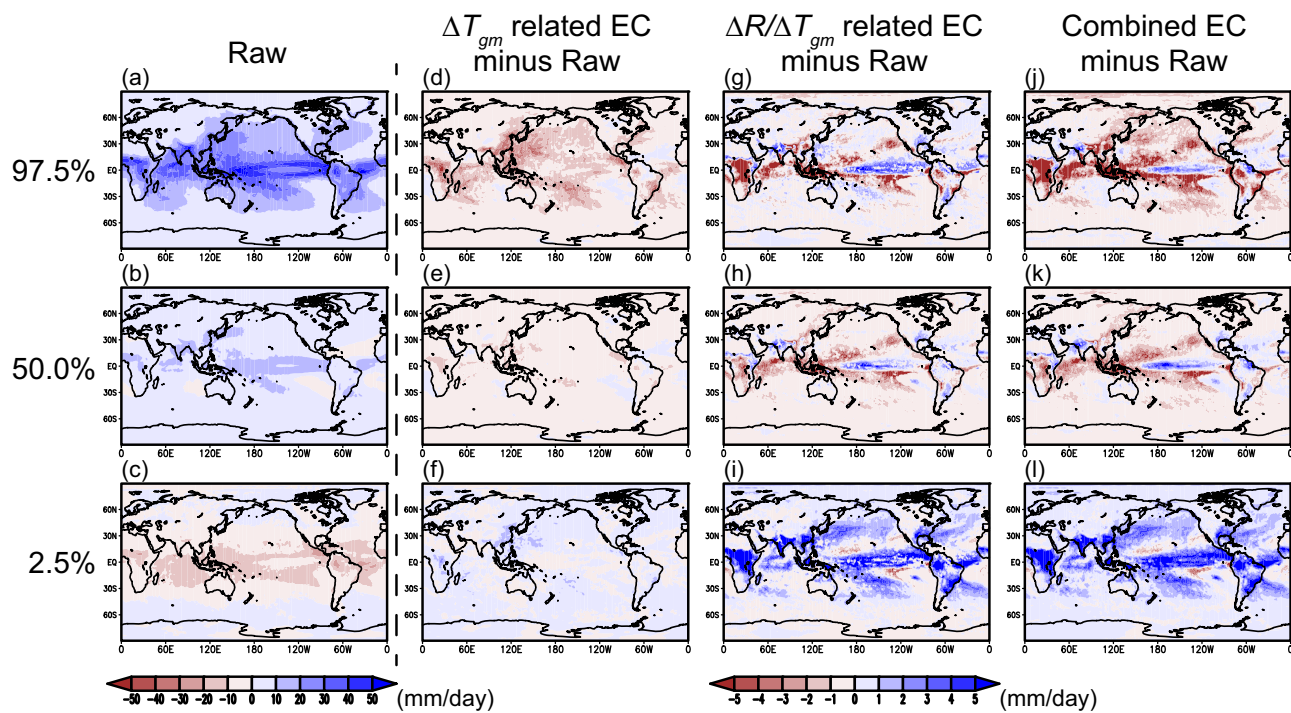


**Fig. 3 | Constraints on the uncertainty ranges of the regional extreme precipitation change ( $\Delta R$ ).** Panels (a–c) show the (a) 97.5th, (b) 50.0th and (c) 2.5th percentiles of the raw projections assuming normal distributions (mm/day). Panels (d–f) indicate the differences between constrained 97.5th, 50.0th and 2.5th

percentile values based on the temperature-related emergent constraint ( $\Delta T_{gm}$ -related EC) and those of the raw projections, respectively (mm/day). Panels (g–i) and (j–l) are the same as (d–f) but for the sensitivity-related ( $\frac{\Delta R_{gm}}{\Delta T_{gm}}$ -related) EC and the combined EC, respectively.

Therefore, the thermodynamic components of regional  $\Delta R$  ( $\Delta R$  due to changes in humidity) are correlated well with  $\Delta T_{gm}$  ( $trT_{gm}$ )<sup>23,24</sup>. The correlations between  $\frac{\Delta R}{\Delta T_{gm}}$  and the past regional  $R$  climatology indicate significant positive values in larger areas than that between  $\Delta R$  and  $trT_{gm}$ . As discussed later, ESMs with higher sensitivity of  $R$  to humidity tend to have larger  $R$  climatology values and greater thermodynamic components of  $\frac{\Delta R}{\Delta T_{gm}}$ , leading to significant correlations between the past  $R$  and  $\frac{\Delta R}{\Delta T_{gm}}$ . There are possibilities of reducing the uncertainties of  $\Delta R$  via our EC methods in areas with significant correlations<sup>23</sup>. The spatial patterns of the correlations between  $\Delta R$  and  $trT_{gm}$  are similar between CMIP5 and CMIP6, but significant correlations are found in larger areas for CMIP6 because the CMIP6 ensemble involves more ‘hot ESMs’ than the CMIP5 ensemble<sup>19,22,23,41,42</sup> (Supplementary Fig. 4). The correlations between the historical  $R$  and  $\frac{\Delta R}{\Delta T_{gm}}$  are similar between CMIP5 and CMIP6.

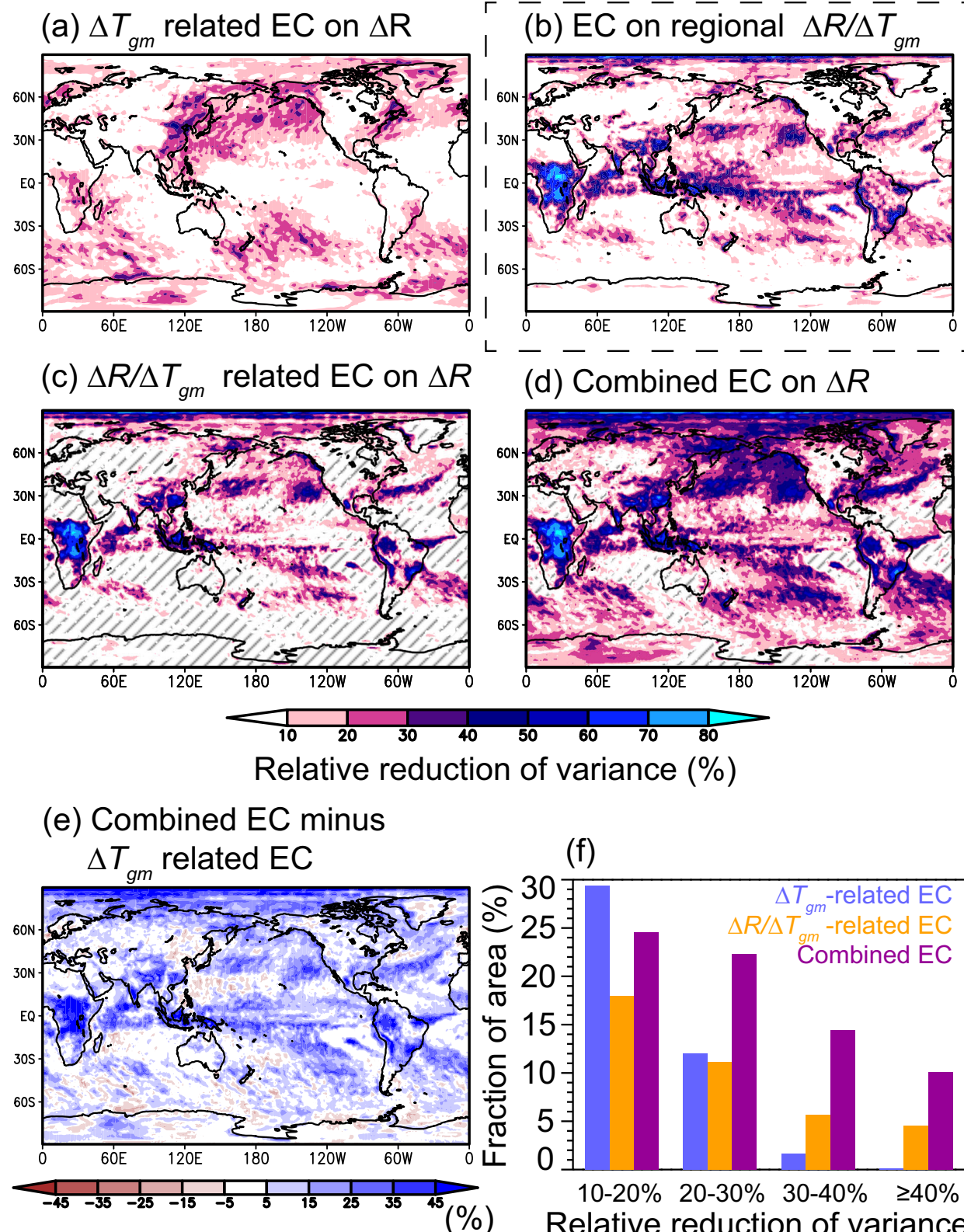
Figure 3 shows changes in the 97.5th, 50th and 2.5th percentile values of  $\Delta R$  owing to our ECs. The  $\Delta T_{gm}$ -related EC lowers the upper bounds of  $\Delta R$  because ESMs with too high  $trT_{gm}$  tend to overestimate  $\Delta R$ <sup>23–26</sup> (Fig. 3d–f). The upper bounds decrease by  $\geq 3$  mm/day in, for example, China, Bangladesh and central Africa. By contrast, the effect of the  $\frac{\Delta R}{\Delta T_{gm}}$ -related EC is more complex (Fig. 3g–i). The  $\frac{\Delta R}{\Delta T_{gm}}$ -related EC increases the lower bounds in many regions by  $\geq 3$  mm/day, such as the storm-track regions in the North Pacific and North Atlantic, East Asia, Southeast Asia, South Asia, Central Africa and South America. The upper bounds decrease by  $\geq 3$  mm/day in, for example, China, Southeast Asia and Central Africa and the subtropical regions of the Pacific Ocean. Both the upper and lower bounds increase in the Intertropical Convergence Zone (ITCZ) of the Pacific and Atlantic Ocean, suggesting that many ESMs underestimate the  $R$  climatology in the ITCZ regions. Although all the global mean ECs do not largely change the 50th percentile values of  $\Delta R_{gm}$ , the  $\frac{\Delta R}{\Delta T_{gm}}$ -related EC cause increases of  $\geq 3$  mm/

day in the ITCZ of the Pacific Ocean and India and decreases in the subtropics of the Pacific Ocean, the Maritime Continent, the Indian Ocean and the Central Africa (Fig. 3h). These opposite changes cancel each other out in the global mean analysis (Fig. 2). The changes in the lower bounds and the median values of the combined EC (Fig. 3k, l) are similar to those in the  $\frac{\Delta R}{\Delta T_{gm}}$ -related EC, because the  $\Delta T_{gm}$ -related EC does not notably affect the lower bounds and median values. By contrast, the pattern of the changes in the upper bounds is a combination of the effects of the  $\Delta T_{gm}$ -related and  $\frac{\Delta R}{\Delta T_{gm}}$ -related ECs (Fig. 3j).

Figure 4 shows the RRVs of the regional  $\Delta R$  and  $\frac{\Delta R}{\Delta T_{gm}}$ . The  $\Delta T_{gm}$ -related EC suppresses the uncertainty in  $\Delta R$  mainly in the middle latitude ocean area and the surrounding coastal regions of both the Northern and Southern Hemispheres (Fig. 4a). The  $\frac{\Delta R}{\Delta T_{gm}}$ -related EC reduces the variance in  $\Delta R$  in, for example, Southeast Asia, China, Central Africa and parts of South America (Fig. 4c). This pattern of RRVs in the  $\frac{\Delta R}{\Delta T_{gm}}$ -related EC on  $\Delta R$  (Fig. 4c) is similar to the RRVs of  $\frac{\Delta R}{\Delta T_{gm}}$  (Fig. 4b), as expected from Eq. 2. The combined EC has a mixed pattern of RRVs between Fig. 4a, c, and reduces the uncertainty in larger areas than only the  $\Delta T_{gm}$ -related EC or the  $\frac{\Delta R}{\Delta T_{gm}}$ -related EC does (Fig. 4d, e).

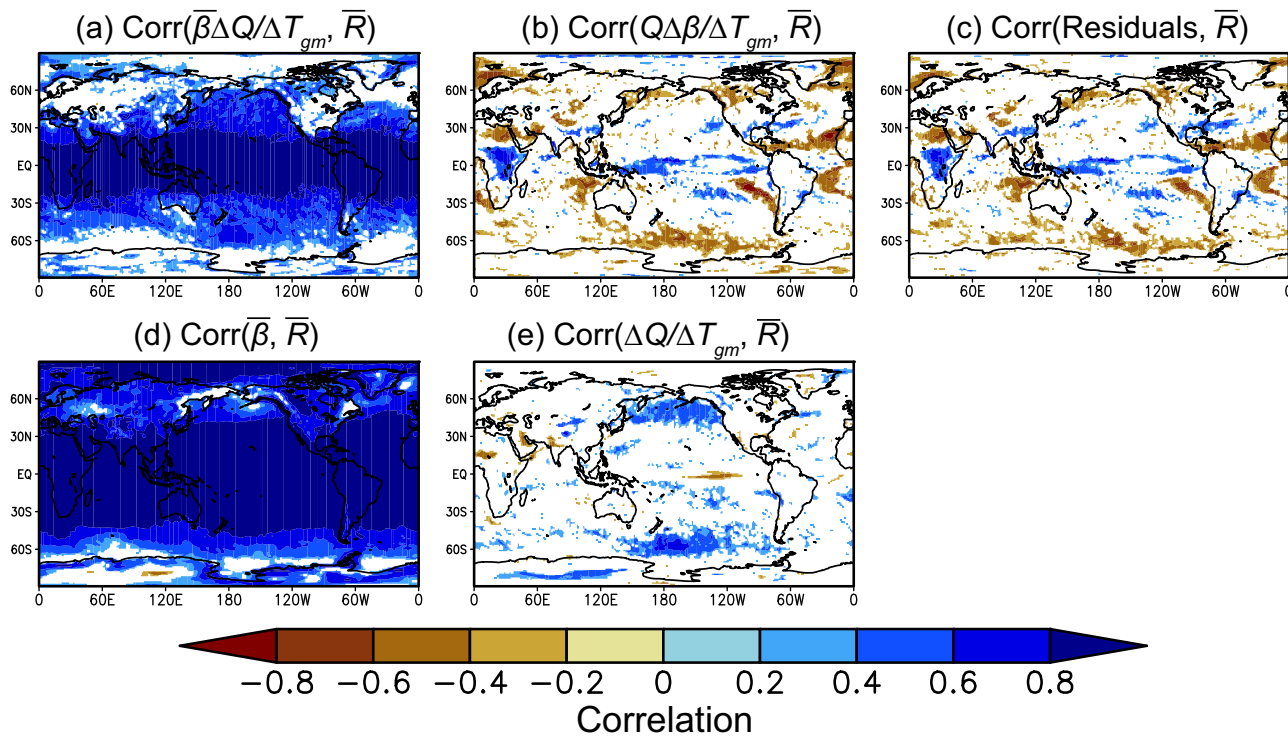
Significant positive correlations between  $\frac{\Delta R}{\Delta T_{gm}}$  and  $\Delta T_{gm}$  are found over, for example, the North Pacific Ocean, the North Atlantic Ocean and the South Pacific Convergence Zone (Supplementary Fig. 5). The understanding of the mechanism for these relationships remains for future work. If we ignored the correlations between  $\frac{\Delta R}{\Delta T_{gm}}$  and  $\Delta T_{gm}$  in our  $\frac{\Delta R}{\Delta T_{gm}}$ -related and combined EC methods, we could overestimate RRVs by 5–25%.

Figure 4f shows the fractions of areas in the world with given ranges of RRV values. By applying the  $\Delta T_{gm}$ -related EC to  $\Delta R$ , we can reduce the variance by 10–20% and 20–30% in 29% and 12% of the global area, respectively, but by  $\geq 30\%$  in only 2% of the global area. The RRVs of the  $\frac{\Delta R}{\Delta T_{gm}}$ -related EC are 10–20%, 20–30%, 30–40% and  $\geq 40\%$  in 17%, 11%, 6% and 4% of the global area, respectively. The combined EC



**Fig. 4 | Reduction of the variance in the regional extreme precipitation change ( $\Delta R$ ).** Shading shows the relative reduction of variance (RRV, %) in the regional  $\Delta R$  (2051–2100 minus 1851–1900) based on (a) the temperature-related emergent constraint ( $\Delta T_{gm}$ -related EC), (c) the sensitivity-related ( $\frac{\Delta R_{gm}}{\Delta T_{gm}}$ -related) EC and (d) the combined EC, respectively. Gray hatches in the panels (c) and (d) indicate where the

RRV becomes negative. In that case, the RRV is set to (c) 0 or (d) the same as that of the  $\Delta T_{gm}$ -related EC (“Methods”). **b** RRV of  $\frac{\Delta R}{\Delta T_{gm}}$  (%). **e** Differences of the RRVs between the combined EC and the  $\Delta T_{gm}$ -related EC (%). **f** Fraction of the global area (%) with RRV values denoted on the horizontal axis for (blue) the  $\Delta T_{gm}$ -related EC, (orange) the  $\frac{\Delta R}{\Delta T_{gm}}$ -related EC and (purple) the combined EC.



**Fig. 5 | Mechanisms underlying the significant correlation between the 1851–1900 mean extreme precipitation ( $\bar{R}$ ) and the extreme precipitation sensitivity ( $\frac{\Delta R}{\Delta T_{gm}}$ ). Correlation between  $\bar{R}$  and (a)  $\bar{\beta} \frac{\Delta Q}{\Delta T_{gm}}$ , (b)  $\bar{Q} \frac{\Delta \beta}{\Delta T_{gm}}$ , (c) residuals of Eq. 5, (d)  $\bar{\beta}$  and (e)  $\frac{\Delta Q}{\Delta T_{gm}}$ .  $Q$  is the specific humidity at 2 m on days when annual maximum daily precipitation events occur.  $\beta = \frac{R}{Q}$  indicates the sensitivity of  $R$  to**

humidity. Overbar denotes the 1851–1900 mean value.  $\bar{\beta} \frac{\Delta Q}{\Delta T_{gm}}$  and  $\bar{Q} \frac{\Delta \beta}{\Delta T_{gm}}$  indicate the thermodynamic and non-thermodynamic (dynamic) components of  $\frac{\Delta R}{\Delta T_{gm}}$ , respectively. The panels (d) and (e) show which of  $\bar{\beta}$  and  $\frac{\Delta Q}{\Delta T_{gm}}$  in the thermodynamic component ( $\bar{\beta} \frac{\Delta Q}{\Delta T_{gm}}$ ) are well related to  $\bar{R}$ . Only significant correlations at the  $\pm 5\%$  levels are drawn.

can most effectively reduce the variance in  $\Delta R$ : the RRVs are 10–20%, 20–30%, 30–40% and  $\geq 40\%$  in 24%, 22%, 14% and 10% of the global area, respectively. The combined method increases RRV even when we employ CMIP5-only, CMIP6-only, RCP8.5/SSP5-8.5 simulations or the different period (1980–2022) for  $trT_{gm}$  (Supplementary Fig. 6a–d). By redoing the EC calculations with each of the ESMs omitted<sup>40</sup>, it is confirmed that the fractions of area are not sensitive to the ESM sampling (Supplementary Fig. 6f).

#### Relationship between $\frac{\Delta R}{\Delta T_{gm}}$ and the past climatology of $R$

To interpret the relationship between  $\frac{\Delta R}{\Delta T_{gm}}$  and the past climatology of  $R$ , we examine specific humidity at 2 m on days when annual maximum daily precipitation events occur ( $Q$ )<sup>23</sup>. Although precipitable water (vertically integrated atmospheric water vapor) is preferable for our purpose, the availability of the precipitable water data from the ESMs is highly limited. We define  $\beta = \frac{R}{Q}$ , which indicates the sensitivity of  $R$  to humidity. Via the definition of  $\beta$ , we can obtain:

$$R = \beta Q \quad (4)$$

We can decompose  $\frac{\Delta R}{\Delta T_{gm}}$  as follows:

$$\frac{\Delta R}{\Delta T_{gm}} = \bar{\beta} \frac{\Delta Q}{\Delta T_{gm}} + \bar{Q} \frac{\Delta \beta}{\Delta T_{gm}} + \text{residuals} \quad (5)$$

where  $\bar{\beta}$  and  $\bar{Q}$  are the averaged  $\beta$  and  $Q$  for the 1851–1900 period, respectively. The 1<sup>st</sup> and 2<sup>nd</sup> terms of the right-hand side represent the thermodynamic and non-thermodynamic (dynamic) components of  $\frac{\Delta R}{\Delta T_{gm}}$ , respectively.

Figure 5a–c show the inter-model correlations between  $\bar{R}$  (the 1851–1900 mean  $R$ ) and each term of the right-hand side of Eq. 5. The

significant positive correlations between  $\frac{\Delta R}{\Delta T_{gm}}$  and the past  $R$  (Supplementary Fig. 4b) mainly result from the high positive correlations between  $\bar{\beta} \frac{\Delta Q}{\Delta T_{gm}}$  and  $\bar{R}$  (Fig. 5a): ESMs with larger  $\bar{R}$  tend to have greater thermodynamic components of  $\frac{\Delta R}{\Delta T_{gm}}$ . Whereas  $\frac{\Delta Q}{\Delta T_{gm}}$  and  $\bar{R}$  have significant correlations in only small area (Fig. 5e),  $\bar{\beta}$  and  $\bar{R}$  have significant positive correlations in most of the world (Fig. 5d), leading to positive correlations between  $\bar{\beta} \frac{\Delta Q}{\Delta T_{gm}}$  and  $\bar{R}$  (Fig. 5a). It is suggested that ESMs with higher sensitivity of extreme precipitation to humidity ( $\bar{\beta}$ ) tend to have both larger extreme precipitation climatology ( $\bar{R}$ ) and greater thermodynamic components of  $\frac{\Delta R}{\Delta T_{gm}}$  ( $\bar{\beta} \frac{\Delta Q}{\Delta T_{gm}}$ ). Therefore, the inter-model variation in the sensitivities of extreme precipitation to humidity is the key factor influencing the significant relationships between  $\frac{\Delta R}{\Delta T_{gm}}$  and the past  $R$  shown in Supplementary Fig. 4b and that between  $\frac{\Delta R_{gm}}{\Delta T_{gm}}$  and the climatology of  $R_{gm}$  shown in Fig. 1c.

The  $\Delta T_{gm}$ -related EC can reduce the uncertainties in the thermodynamic components of  $\Delta R$ , but not the dynamic components of  $\Delta R$ <sup>23,24</sup>. Therefore the RRVs for the  $\Delta T_{gm}$ -related EC on  $\Delta R$  are small over the tropical ocean where the contributions of dynamic components to  $\Delta R$  are large<sup>23,24</sup> (Fig. 4a). By contrast, the RRVs for the  $\frac{\Delta R}{\Delta T_{gm}}$ -related EC on  $\Delta R$  are large in the major precipitation regions in the world, e.g., the ITCZ in the tropics, the storm-track regions in the middle latitude and the Asian monsoon region (Fig. 4c), because the sensitivities of extreme precipitation to humidity are the important factor for the intensities of  $R$  worldwide (Fig. 5a, d). The  $\frac{\Delta R}{\Delta T_{gm}}$ -related EC can reduce the uncertainty of  $\Delta R$  in the tropical ocean regions, where the  $\Delta T_{gm}$ -related EC is not effective (Fig. 4a, c). In the middle and high latitudes, both the  $\Delta T_{gm}$ -related and  $\frac{\Delta R}{\Delta T_{gm}}$ -related ECs can reduce the uncertainties of  $\Delta R$ . The combined

EC is effective because the two ECs complement and strengthen each other (Fig. 4d, e).

## Discussion

Recently,  $\Delta T_{gm}$ -related ECs have attracted increasing attention and have been applied to constrain several climate variables, extreme indices, the carbon cycle and the economic impact of climate change<sup>22–28</sup>. Although  $\Delta T_{gm}$ -related ECs are a useful approach, such ECs can reduce only the  $\Delta T_{gm}$ -related uncertainty in climate change projections. To overcome this limitation, we develop a method that combines the EC on  $\Delta T_{gm}$  and the sensitivity-related EC, and more efficiently constrain the uncertainties in global mean and regional annual maximum daily precipitation changes than the  $\Delta T_{gm}$ -related EC can. The combined EC can reduce the inter-model variance in  $\Delta R_{gm}$  by 42%, whereas it is 26% in the  $\Delta T_{gm}$ -related EC. Although the  $\Delta T_{gm}$ -related EC can reduce the variance in the regional  $\Delta R$  by  $\geq 30\%$  in only 2% of the global area, the combined EC reduces the variance by  $\geq 30\%$  in 24% of the global area.

Note that our ECs on  $\frac{\Delta R_{gm}}{\Delta T_{gm}}$  and  $\frac{\Delta R}{\Delta T_{gm}}$  are also epochal. Although two studies have provided ECs on extreme precipitation sensitivity<sup>43,44</sup>, one of them<sup>44</sup> is not robust for the CMIP6 ESMs<sup>45</sup>, and the applicable area of the remaining one is limited to the tropical ocean<sup>43</sup>. Our ECs are applicable across a wide area (Fig. 4) and are robust for both the CMIP5 and CMIP6 (Supplementary Figs. 3 and 6). The large uncertainty in the observed precipitation datasets (Fig. 1c and Supplementary Fig. 7, “Methods”) is a factor limiting more effective uncertainty reduction via the  $\frac{\Delta R}{\Delta T_{gm}}$ -related and combined ECs. Therefore, improvements in the observed datasets are warranted for obtaining more effective constraints on future extreme precipitation changes. Previous studies<sup>23–26</sup> applied  $\Delta T_{gm}$ -related ECs on percentage changes in extreme precipitation intensity (changes in extreme precipitation divided by their past mean values) but not  $\Delta R$ . Dividing  $\frac{\Delta R}{\Delta T_{gm}}$  by the mean  $R$  ( $\frac{1}{\text{mean}R} \times \frac{\Delta R}{\Delta T_{gm}}$ ) makes it hard to use the information of the biases of the mean  $R$ , because it is not good that both the predictand ( $\frac{1}{\text{mean}R} \times \frac{\Delta R}{\Delta T_{gm}}$ ) and the predictor (mean  $R$ ) of the EC method involve the same information of the mean  $R$ . To improve EC methods, meticulous care must be taken in selecting not only predictors but also predictands.

Thackeray et al.<sup>12</sup> proposed a different EC on future changes in magnitude and frequency of extreme precipitation (daily precipitation  $\geq 99^{\text{th}}$  percentile) using their relationships with trends in the frequency of extreme precipitation over recent decades. They found that ESMs with higher increases in the frequency of extreme precipitation in recent decades tend to have greater increases in magnitude and frequency of extreme precipitation in the future. They suggested that their EC using the recent trends in the frequency of extreme precipitation led to stronger constraints on future changes in the frequency of extreme precipitation than an EC using historical warming, especially for the CMIP5 ensemble. If the recent trends in the frequency of extreme precipitation offer some independent information than  $trT_{gm}$  and the mean  $R$ , there is a possibility to improve ECs on  $\Delta R$ . A method was developed for integrating information from several ECs on a single indicator, i.e., climate sensitivity<sup>40</sup>. The integration of ECs on the extreme precipitation intensity from Thackeray et al.<sup>12</sup> and this study may provide further reliable assessments.

Our combined EC approach can be applied to changes in other climate variables, extreme indices and circulation to reduce their uncertainties. Although combined ECs should encompass ECs on sensitivities to  $1^{\circ}\text{C}$  of global warming, previous studies have already provided ECs on the sensitivity of, for example, water resources in South America<sup>15</sup>, tropical land carbon storage<sup>46</sup> and tropical ocean primary production<sup>47</sup>. Our combined EC approach potentially enhances uncertainty reductions and can help inform mitigation and adaptation policies.

## Methods

### CMIP5 and CMIP6 ESM simulations

We analyze the historical (1851–2005 for the CMIP5 and 1851–2014 for the CMIP6) and future (up to 2100, RCP4.5 (RCP8.5) for the CMIP5 and SSP2-4.5 (SSP5-8.5) for the CMIP6) simulations of 56 ESMs (Supplementary Table 1). In the historical simulations, ESMs are forced by historical changes in anthropogenic (greenhouse gas concentrations, aerosol emissions, ozone concentrations and land use) and natural (solar irradiance and volcanic activity) external forcing factors. RCP4.5 and SSP2-4.5 (RCP8.5 and SSP5-8.5) are future scenarios for greenhouse gas concentrations, anthropogenic aerosol emissions, ozone concentrations and land use. We mainly analyze the ensemble average of each ESM. We calculate the annual maximum daily precipitation ( $R$ ), annual mean temperature ( $T$ ) and specific humidity at 2 m for days when  $R$  events occur ( $Q$ ) in the original grids of ESMs, and then interpolate those to  $1^{\circ}$  latitude  $\times$   $1^{\circ}$  longitude grids.

### Uncertainty ranges of the observed $trT_{gm}$ values

As in ref. 34, we calculate the 1970–2022 trends in the global mean temperature ( $trT_{gm}$ ) from the ESMs and the observations. We examine  $trT_{gm}$  of the 200 member realizations of the HadCRUT5 observed temperature datasets<sup>33</sup>. The variation between these realizations represents uncertainties resulting from systematic errors associated with observational methods, measurement and sampling errors and spatial analysis uncertainty. To consider the blending effect of the surface air temperature over land and ice and the sea-surface temperature over the ocean,  $0.014^{\circ}\text{C}/10\text{-years}$ <sup>19</sup> is added to the  $trT_{gm}$  values of HadCRUT5. The average and standard deviation of the 200 HadCRUT5 realizations are  $0.208^{\circ}\text{C}/10\text{-years}$  and  $0.00267^{\circ}\text{C}/10\text{-years}$ , respectively. To consider the uncertainty stemming from the internal climate variability in the observed  $trT_{gm}$ , we employ  $trT_{gm}$  data from 25-members  $\times$  5-ESMs of the CMIP6 (historical (1970–2014) + SSP2-4.5 (2015–2022)) (Supplementary Table 1). For each ESM, we compute anomalies from their 25-member average. The standard deviation of those anomalies is  $0.0179^{\circ}\text{C}/10\text{-years}$ . The standard deviation accounting for both the difference between the HadCRUT5 realizations and the internal variability is  $0.0181^{\circ}\text{C}/10\text{-years}$  ( $= \sqrt{0.00267^2 + 0.0179^2}$ ). We consider the uncertainty range of the observed  $trT_{gm}$  values, as indicated by the blue horizontal bars in Fig. 1a, b, by using a normal distribution with a mean of  $0.208^{\circ}\text{C}/10\text{-years}$  and a standard deviation of  $0.0181^{\circ}\text{C}/10\text{-years}$ . As a sensitivity test, we also double the variance of the internal variability: the total standard deviation is  $0.0254^{\circ}\text{C}/10\text{-years}$  ( $= \sqrt{0.00267^2 + 0.0179^2 \times 2}$ ), as indicated by the green horizontal bars in Fig. 1a, b.

### Uncertainty range of the observed $R$ values

We employ three observational datasets of the global daily precipitation: GPCP<sup>36</sup>, MSWEP2 (V2.80)<sup>37</sup> and GSWP3-WSE5<sup>38,39</sup>. GPCP is a merged dataset of gauge stations, satellites and sounding observations. MSWEP2 is a merged dataset of gauge-, satellite- and reanalysis-based data. GSWP3-WSE5 is the combined dataset of GSWP3 (a merged dataset of dynamically downscaled twentieth-century reanalysis data and global observations of precipitation) and WSE5 (a merged dataset of bias-adjusted and raw reanalysis datasets). The differences between the observational datasets of precipitation are large due to many sources of uncertainty<sup>48,49</sup>, e.g., limited number and spatial coverage of surface stations, and differences in satellite algorithms, data assimilation methods, reanalysis datasets and bias correction methods. The 1997–2019 mean  $R_{gm}$  values of these datasets are 33.8, 48.2, and 44.9 mm/day (their standard errors of the mean values due to the interannual variations are 0.479, 0.307 and 0.329 mm/day), respectively. The average and standard deviation of these three mean values are 42.3 and 7.55 mm/day, respectively. The standard deviation of the 25-members  $\times$  5-ESMs (using anomalies from the 25-member-mean for

each ESM) is 0.142 mm/day. The total standard deviation (estimated from the variations between the three observed datasets and the internal variability in the 25-members  $\times$  5-ESMs) used in Fig. 1c is 7.55 ( $=\sqrt{7.55^2+0.142^2}$ ) mm/day. For Figs. 3 and 4, the average and total standard deviation values of the 1997–2019 mean  $R$  in each grid are used. In most parts of the world, the inter-observational-datasets variance dominates the total variance (inter-observational-datasets + internal climate variability) of the 1997–2019 mean  $R$  (Supplementary Fig. 7).

### Emergent constraints on single variables

By assuming **normal distributions** of the ESM spreads, we estimate the raw uncertainty ranges of future change projections. Note that long-term and/or globally averaged values of future changes match Gaussian distributions well in most cases because of the central limit theorem<sup>23</sup>. We apply the hierarchical EC framework<sup>22</sup> to calculate the observationally constrained ranges of the changes in single variables. Here,  $\mathbf{z}$  denotes future changes ( $\Delta R_{gm}$ ,  $\Delta T_{gm}$ ,  $\frac{\Delta R_{gm}}{\Delta T_{gm}}$ ,  $\Delta R$ , or  $\frac{\Delta R}{\Delta T_{gm}}$ ).  $\mu_z$  and  $\delta_z$  are the ensemble mean and standard deviation of  $\mathbf{z}$ , respectively.  $\mathbf{x}$  indicates historical metrics of the ESMs used for the ECs (i.e.,  $trT_{gm}$ , the 1997–2019 mean  $R_{gm}$ , or the 1997–2019 mean  $R$ ).  $\mu_x$  and  $\delta_x$  are the ensemble mean and standard deviation of  $\mathbf{x}$ , respectively. The correlation between  $\mathbf{z}$  and  $\mathbf{x}$  is denoted by  $\rho$ .  $\mu_y$  and  $\delta_y$  indicate the abovementioned mean and the standard deviation values of the observations ( $\mathbf{y}$ ), respectively.

The mean ( $E(\mathbf{z}|\mathbf{y})$ ) and standard deviation ( $\delta(\mathbf{z}|\mathbf{y})$ ) of the constrained future projections are estimated as follows:

$$E(\mathbf{z}|\mathbf{y}) = \mu_z + \frac{\rho \delta_z \delta_x}{\delta_x^2 + \delta_y^2} (\mu_y - \mu_x) \quad (6)$$

$$\delta(\mathbf{z}|\mathbf{y}) = \delta_z \sqrt{1 - \frac{\rho^2}{1 + (\delta_y^2/\delta_x^2)}} \quad (7)$$

By assuming a normal distribution with  $E(\mathbf{z}|\mathbf{y})$  and  $\delta(\mathbf{z}|\mathbf{y})$ , we estimate the constrained range of  $\mathbf{z}$ . The relative reduction of variance (RRV) is calculated as follows:

$$RRV = \left(1 - \frac{\delta^2(\mathbf{z}|\mathbf{y})}{\delta_z^2}\right) \times 100\% \quad (8)$$

If  $\rho$  is small, RRV becomes close to zero.

### Combined emergent constraints

We define  $m_{raw}(z)$  and  $s_{raw}(z)$  as the raw mean and standard deviation of future changes,  $z$ , respectively. Here,  $z = \Delta T_{gm}$  or  $\frac{\Delta R_{gm}}{\Delta T_{gm}}$ .  $m_{con}(z)$  and  $s_{con}(z)$  are the mean and standard deviation of constrained future changes, respectively. The inter-model correlation between  $\frac{\Delta R_{gm}}{\Delta T_{gm}}$  and  $\Delta T_{gm}$  is denoted as  $r_0$ .

We employ the constrained  $\frac{\Delta R_{gm}}{\Delta T_{gm}}$  and the raw  $\Delta T_{gm}$  to apply the  $\frac{\Delta R_{gm}}{\Delta T_{gm}}$ -related EC on  $\Delta R_{gm}$ . We define  $\mathbf{v}_1 = [\text{constrained } \frac{\Delta R_{gm}}{\Delta T_{gm}}, \text{raw } \Delta T_{gm}]^T$ . The covariance matrix of the constrained  $\frac{\Delta R_{gm}}{\Delta T_{gm}}$  and the raw  $\Delta T_{gm}$  ( $\Pi_1$ ) can be estimated as:

$$\Pi_1 = \begin{bmatrix} s_{con}^2\left(\frac{\Delta R_{gm}}{\Delta T_{gm}}\right) & r_0 s_{con}\left(\frac{\Delta R_{gm}}{\Delta T_{gm}}\right) s_{raw}(\Delta T_{gm}) \\ r_0 s_{con}\left(\frac{\Delta R_{gm}}{\Delta T_{gm}}\right) s_{raw}(\Delta T_{gm}) & s_{raw}^2(\Delta T_{gm}) \end{bmatrix} \quad (9)$$

The joint normal distribution of  $\mathbf{v}_1$  is as follows:

$$\mathbf{v}_1 \sim \mathcal{N} \left( \left[ m_{con}\left(\frac{\Delta R_{gm}}{\Delta T_{gm}}\right), m_{raw}(\Delta T_{gm}) \right]^T, \Pi_1 \right). \quad (10)$$

We randomly sample  $\mathbf{v}_1$  by using the joint normal distribution of Eq. 10 and compute  $\Delta R_{gm} = \left(\frac{\Delta R_{gm}}{\Delta T_{gm}}\right)\Delta T_{gm}$  from  $\mathbf{v}_1$  10000 times. Then, we estimate the 2.5th, 50th and 97.5th percentile values of the 10000 samples of  $\Delta R_{gm}$  as the constrained uncertainty range of the  $\frac{\Delta R_{gm}}{\Delta T_{gm}}$ -related EC, and calculate the RRV by using the standard deviation of the 10000 samples.

To apply the combined EC, the raw  $\Delta T_{gm}$  of the abovementioned method is replaced by the constrained  $\Delta T_{gm}$ . We define  $\mathbf{v}_2 = [\text{constrained } \frac{\Delta R_{gm}}{\Delta T_{gm}}, \text{constrained } \Delta T_{gm}]^T$ . The covariance matrix of constrained  $\frac{\Delta R_{gm}}{\Delta T_{gm}}$  and  $\Delta T_{gm}$  ( $\Pi_2$ ) can be estimated as:

$$\Pi_2 = \begin{bmatrix} s_{con}^2\left(\frac{\Delta R_{gm}}{\Delta T_{gm}}\right) & r_0 s_{con}\left(\frac{\Delta R_{gm}}{\Delta T_{gm}}\right) s_{con}(\Delta T_{gm}) \\ r_0 s_{con}\left(\frac{\Delta R_{gm}}{\Delta T_{gm}}\right) s_{con}(\Delta T_{gm}) & s_{con}^2(\Delta T_{gm}) \end{bmatrix} \quad (11)$$

The joint normal distribution of  $\mathbf{v}_2$  is as follows:

$$\mathbf{v}_2 \sim \mathcal{N} \left( \left[ m_{con}\left(\frac{\Delta R_{gm}}{\Delta T_{gm}}\right), m_{con}(\Delta T_{gm}) \right]^T, \Pi_2 \right) \quad (12)$$

We randomly sample  $\mathbf{v}_2$  by using the joint normal distribution of Eq. 12 and compute  $\Delta R_{gm} = \left(\frac{\Delta R_{gm}}{\Delta T_{gm}}\right)\Delta T_{gm}$  from  $\mathbf{v}_2$  10000 times. Then we estimate the 2.5th, 50th and 97.5th percentile values of the 10000 samples of  $\Delta R_{gm}$  as the constrained uncertainty range of the combined EC, and determine the RRV by using the standard deviation of the 10000 samples.

For the regional ECs,  $\Delta R_{gm}$  and  $\frac{\Delta R_{gm}}{\Delta T_{gm}}$  in the above equations, are replaced by  $\Delta R$  and  $\frac{\Delta R}{\Delta T_{gm}}$ , respectively. While the ECs on single variables do not yield negative RRVs according to the definition of Eqs. 7, 8, the  $\frac{\Delta R}{\Delta T_{gm}}$ -related EC and the combined EC on  $\Delta R$  can have negative RRVs (as marked by hatches in Fig. 4c, d). Because negative RRVs indicate that ECs increase the uncertainty, we do not have to apply ECs in that case. Therefore, in the grids with negative RRVs, we replace the constrained ranges of the  $\frac{\Delta R}{\Delta T_{gm}}$ -related EC and the combined EC by the raw ranges (RRVs = 0) and the constrained ranges of the  $\Delta T_{gm}$ -related EC (the RRVs are the same as that of the  $\Delta T_{gm}$ -related EC), respectively.

### Baseline period

If we use the recent past period (1970–2022) as the baseline instead of the 1851–1900 period, RRVs become smaller. The RRVs of the  $\Delta T_{gm}$ -related,  $\frac{\Delta R_{gm}}{\Delta T_{gm}}$ -related and combined ECs on the global mean  $\Delta R_{gm}$  change from 26%, 27% and 42% to 23%, 25% and 41%, respectively (Fig. 2 and Supplementary Fig. 3e). The combined EC decreases the variance of regional  $\Delta R$  by  $\geq 30\%$  in 12% of the global area for the 1970–2022 baseline case, while it is 24% for the 1851–1900 baseline case (Fig. 4f and Supplementary Fig. 6e). These decreases of RRVs are caused by the two factors: (i) the declines of aerosol emissions from the recent past period to the future period affect  $\Delta T_{gm}$ ,  $\Delta R_{gm}$  and  $\Delta R$  in the 1970–2022 baseline case; (ii) the magnitudes of  $\Delta T_{gm}$ ,  $\Delta R_{gm}$  and  $\Delta R$  relative to the 1970–2022 mean are smaller than that relative to the 1851–1900 mean. Because  $trT_{gm}$  is the metric for ECs on future climate responses to increases in greenhouse gas concentrations but not for climate responses to changes in aerosol emissions<sup>18,19,22</sup>, we select the 1851–1900 period as the baseline.

## Data availability

All data that support the findings of this study are available from the following: CMIP5: <https://esgf-node.llnl.gov/search/cmip5/> (last access, 27 Sept. 2024). CMIP6: <https://esgf-node.llnl.gov/search/cmip6/> (last access, 27 Sept. 2024). HadCRUT5: <https://www.metoffice.gov.uk/hadobs/hadcrut5/> (last access, 27 Sept. 2024). GPCP: <https://www.ncei.noaa.gov/products/climate-data-records/precipitation-gpcp-daily> (last access, 27 Sept. 2024). MSWEP2 (v2.80): <http://www.globo20.org/> (last access, 27 Sept. 2024). GSWP3-WSE5: <https://www.isimip.org/gettingstarted/input-data-bias-adjustment/details/110/> (last access, 27 Sept. 2024)

## Code availability

The codes are available from <https://doi.org/10.6084/m9.figshare.28283093>.

## References

1. IPCC 2022, Summary for Policymakers. in *Climate Change 2022: Impacts, Adaptation, and Vulnerability.*(Cambridge University Press, 2022).
2. IPCC. Summary for Policymakers. in *Climate Change 2021: The Physical Science Basis. Contribution of Working Group I to the Sixth Assessment Report of the Intergovernmental Panel on Climate Change.* (2021).
3. Swiss Re Institute. Natural catastrophes in 2021: the floodgates are open. *Sigma*, No 1/2022 (2022).
4. Min, S. K., Zhang, X., Zwiers, F. W. & Hegerl, G. C. Human contribution to more-intense precipitation extremes. *Nature* **470**, 378–381 (2011).
5. Shiogama, H. et al. Attributing historical changes in probabilities of record-breaking daily temperature and precipitation extreme events. *SOLA* **12**, 225–231 (2016).
6. Dong, S. et al. Attribution of extreme precipitation with updated observations and CMIP6 simulations. *J. Clim.* **34**, 871–881 (2021).
7. Sugiyama, M., Shiogama, H. & Emori, S. Precipitation extreme changes exceeding moisture content increases in MIROC and IPCC climate models. *Proc. Natl. Acad. Sci. USA* **107**, 571–575 (2010).
8. O’Gorman, P. A. & Schneider, T. The physical basis for increases in precipitation extremes in simulations of 21<sup>st</sup>-century climate change. *Proc. Natl. Acad. Sci. USA* **106**, 14773–14777 (2009).
9. Polade, S. D. et al. The key role of dry days in changing regional climate and precipitation regimes. *Sci. Rep.* **4**, 4364 (2014).
10. Pfahl, S., O’Gorman, P. A. & Fischer, E. M. Understanding the regional pattern of projected future changes in extreme precipitation. *Nat. Clim. Chang* **7**, 423–428 (2017).
11. Shiogama, H. et al. How many hot days and heavy precipitation days will grandchildren experience that break the records set in their grandparents’ lives? *Environ. Res. Commun.* **3**, 061002 (2021).
12. Thackeray, C. W., Hall, A., Norris, J. & Chen, D. Constraining the increased frequency of global precipitation extremes under warming. *Nat. Clim. Chang* **12**, 441–448 (2022).
13. Knutti, R. The end of model democracy? *Clim. Chang* **102**, 395–404 (2010).
14. Hall, A. & Qu, X. Using the current seasonal cycle to constrain snow albedo feedback in future climate change. *Geophys. Res. Lett.* **33**, L03502 (2006).
15. Shiogama, H. et al. Observational constraints indicate risk of drying in the Amazon basin. *Nat. Commun.* **2**, 253 (2011).
16. Hall, A. et al. Progressing emergent constraints on future climate change. *Nat. Clim. Chang.* **9**, 269–278 (2019).
17. Brent, F. Reducing Uncertainties in Climate Projections with Emergent Constraints: Concepts, Examples and Prospects. *Adv. Atmos. Sci.* **37**, 1–15 (2020).
18. Jiménez-de-la-Cuesta, D. & Mauritsen, T. Emergent constraints on Earth’s transient and equilibrium response to doubled CO<sub>2</sub> from post-1970s global warming. *Nat. Geosci.* **12**, 902–905 (2019).
19. Tokarska, K. B. et al. Past warming trend constrains future warming in CMIP6 models. *Sci. Adv.* **6**, eaaz9549 (2020).
20. Nijssse, F. J. M. M., Cox, P. M. & Williamson, M. S. Emergent constraints on transient climate response (TCR) and equilibrium climate sensitivity (ECS) from historical warming in CMIP5 and CMIP6 models. *Earth Syst. Dynam.* **11**, 737–750 (2020).
21. Liang, Y., Gillett, N. P. & Monahan, A. H. Climate model projections of 21<sup>st</sup> century global warming constrained using the observed warming trend. *Geophys. Res. Lett.* **47**, e2019GL086757 (2020).
22. Shiogama, H., Watanabe, M., Kim, H. & Hirota, N. Emergent constraints on future precipitation changes. *Nature* **602**, 612–616 (2022).
23. Shiogama, H., Hayashi, M., Hirota, N. & Ogura, T. Emergent constraints on future changes in several climate variables and extreme indices from global to regional scales. *Sci. Online Lett. Atmos.* **20**, 122–129 (2024).
24. Paik, S., An, S., Min, S., King, A. & Kim, S. Emergent constraints on future extreme precipitation intensification: from global to continental scales. *Weather. Clim. Extrem.* **42**, 100613 (2023).
25. Li, C. et al. Constraining projected changes in rare intense precipitation events across global land regions. *Geophys. Res. Lett.* **51**, e2023GL105605 (2024).
26. Dai, P. et al. Constraints on regional projections of mean and extreme precipitation under warming. *Proc. Natl. Acad. Sci. USA* **121**, e2312400121 (2024).
27. Melnikova, I. et al. Emergent constraints on future Amazon climate change-induced carbon loss using past global warming trends. *Nat. Commun.* **15**, 7623 (2024).
28. Shiogama, H., Takakura, J. & Takahashi, K. Uncertainty constraints on economic impact assessments of climate change simulated by an impact emulator. *Environ. Res. Lett.* **17**, 124028 (2022).
29. Taylor, K. E., Stouffer, R. J. & Meehl, G. A. An Overview of CMIP5 and the experiment design. *Bull. Amer. Meteor. Soc.* **93**, 485–498 (2012).
30. Eyring, V. et al. Overview of the coupled model intercomparison project phase 6 (CMIP6) experimental design and organization. *Geosci. Model Dev.* **9**, 1937–1958 (2016).
31. O’Neill, B. C. et al. A new scenario framework for climate change research: the concept of shared socioeconomic pathways. *Clim. Chang* **122**, 387–400 (2014).
32. Bowman, K. W., Cressie, N., Qu, X. & Hall, A. A hierarchical statistical framework for emergent constraints: application to snow-albedo feedback. *Geophys. Res. Lett.* **45**, 13050–13059 (2018).
33. Morice, C. P. et al. An updated assessment of near-surface temperature change from 1850: the HadCRUT5 data set. *J. Geophys. Res. Atmos.* **126**, e2019JD032361 (2021).
34. Liang, Y., Gillett, N. P. & Monahan, A. H. Accounting for Pacific climate variability increases projected global warming. *Nat. Clim. Chang.* **14**, 608–614 (2024).
35. Watanabe, M. et al. Possible shift in controls of the tropical Pacific surface warming pattern. *Nature* **630**, 315–324 (2024).
36. Adler, R. et al. The global precipitation climatology project (GPCP) monthly analysis (New Version 2.3) and a review of 2017 global precipitation. *Atmosphere* **9**, 138 (2018).
37. Beck, H. E. et al. MSWEP V2 global 3-hourly 0.1° precipitation: methodology and quantitative assessment. *Bull. Amer. Meteor. Soc.* **100**, 473–500 (2019).
38. Kim, H. Global Soil Wetness Project Phase 3 Atmospheric Boundary Conditions (Experiment 1) [Data set]. Data Integration and Analysis System (DIAS). <https://doi.org/10.20783/DIAS.501> (2017).

39. Lange, S. et al. WFDE5 over land merged with ERA5 over the ocean (W5E5 v2.0). ISIMIP Repository. <https://doi.org/10.48364/ISIMIP.342217> (2021).
40. Bretherton, C. S. & Caldwell, P. M. Combining emergent constraints for climate sensitivity. *J. Clim.* **33**, 7413–7430 (2020).
41. Zelinka, M. D. et al. Causes of higher climate sensitivity in CMIP6 models. *Geophys. Res. Lett.* **47**, e2019GL085782 (2020).
42. Hausfather, Z. et al. Climate simulations: Recognize the 'hot model' problem. *Nature* **605**, 26–29 (2022).
43. O'Gorman, P. A. Sensitivity of tropical precipitation extremes to climate change. *Nat. Geosci.* **5**, 697–700 (2012).
44. Borodina, A., Fischer, E. M. & Knutti, R. Models are likely to underestimate increase in heavy rainfall in the extratropical regions with high rainfall intensity. *Geophys. Res. Lett.* **44**, 7401–7409 (2017).
45. Fergulja, O., von Hardenberg, J. & Palazzi, E. Robustness of precipitation emergent constraints in CMIP6 models. *Clim. Dyn.* **61**, 1439–1450 (2023).
46. Wenzel, S., Cox, P. M., Eyring, V. & Friedlingstein, P. Emergent constraints on climate-carbon cycle feedbacks in the CMIP5 Earth system models. *J. Geophys. Res. Biogeosci.* **119**, 794–807 (2014).
47. Kwiatkowski, L. et al. Emergent constraints on projections of declining primary production in the tropical oceans. *Nat. Clim. Change* **7**, 355–358 (2017).
48. Sun, Q. et al. A review of global precipitation data sets: data sources, estimation, and intercomparisons. *Rev. Geophys.* **56**, 79–107 (2018).
49. Kobayashi, S. et al. The JRA-55 reanalysis: general specifications and basic characteristics. *J. Meteorol. Soc. Jpn* **93**, 5–48 (2015).

## Acknowledgements

This work was supported by the Advanced Studies of Climate Change Projection (SENTAN, JPMXD0722680395) of the Ministry of Education, Culture, Sports, Science and Technology of Japan (H.S., M.H., N.H., T.O., and M.W.); the Environment Research and Technology Development Fund (JPMEERF20242001) of the Environmental Restoration and Conservation Agency and the Ministry of Environment of Japan (H.S., M.H., and N.H.); and the National Research Foundation of Korea (NRF) grant (RS-2025-02312954 and RS-2021-NR055516) of the Korea Government (MSIT) (H.K.).

## Author contributions

H.S. mainly performed the analyses and wrote the paper. H.S., M.H., and N.H. collected the data. H.K. provided information about the uncertainty

in the observational datasets. M.H., N.H., T.O., and M.W. provided insights about ECs on temperature and precipitation. All the authors discussed the results and commented on the manuscript.

## Competing interests

The authors declare no financial or non-financial competing interests.

## Additional information

**Supplementary information** The online version contains supplementary material available at <https://doi.org/10.1038/s41467-025-60385-1>.

**Correspondence** and requests for materials should be addressed to Hideo Shiogama.

**Peer review information** *Nature Communications* thanks Chad Thackeray and the other anonymous reviewer for their contribution to the peer review of this work. A peer review file is available.

**Reprints and permissions information** is available at <http://www.nature.com/reprints>

**Publisher's note** Springer Nature remains neutral with regard to jurisdictional claims in published maps and institutional affiliations.

**Open Access** This article is licensed under a Creative Commons Attribution-NonCommercial-NoDerivatives 4.0 International License, which permits any non-commercial use, sharing, distribution and reproduction in any medium or format, as long as you give appropriate credit to the original author(s) and the source, provide a link to the Creative Commons licence, and indicate if you modified the licensed material. You do not have permission under this licence to share adapted material derived from this article or parts of it. The images or other third party material in this article are included in the article's Creative Commons licence, unless indicated otherwise in a credit line to the material. If material is not included in the article's Creative Commons licence and your intended use is not permitted by statutory regulation or exceeds the permitted use, you will need to obtain permission directly from the copyright holder. To view a copy of this licence, visit <http://creativecommons.org/licenses/by-nc-nd/4.0/>.

© The Author(s) 2025